Possible polymetamorphism and brine infiltration recorded in the garnet-sillimanite gneiss, Skallevikshalsen, Lützow-Holm Complex, East Antarctica

Tetsuo Kawakami[*], Tomokazu Hokada[**,***], Shuhei Sakata[*] and Takafumi Hirata[*]

[*]*Department of Geology and Mineralogy, Graduate School of Science, Kyoto University, Kyoto 606-8502, Japan*
[**]*National Institute of Polar Research, Tachikawa, Tokyo 190-8518, Japan*
[***]*Department of Polar Science, The Graduate University for Advanced Studies, Tachikawa, Tokyo 190-8518, Japan*

Chlorine-rich (>0.3 wt%Cl) biotite inclusions in the core of garnet porphyroblasts in the garnet-sillimanite (Grt-Sil) gneiss from Skallevikshalsen, Lützow-Holm Complex (LHC), East Antarctica is estimated to be stable under >1.2 GPa, 820-850 °C, coexisted with granitic melt as suggested by the nanogranite/felsite inclusions. Rare occurrence of matrix biotite, in spite of the common occurrence of biotite as inclusions in garnet, suggests almost complete consumption of pre-existed matrix biotite during the prograde to peak metamorphism. Brine infiltration during prograde to peak metamorphism in Skallevikshalsen is supported by Cl-rich scapolite described in previous studies. Brine infiltration and progress of continuous biotite-consuming melting reactions were probably responsible for elevating the Cl content of biotite in the studied sample.

In situ electron microprobe U-Th-Pb dating of monazite and the in situ laser ablation inductively coupled plasma mass spectrometry (LA-ICPMS) U-Pb dating of zircon in the Grt-Sil gneiss revealed that both monazite and zircon has the 'older age population' with ~ 650-580 Ma and the 'younger age population' with ~ 560-500 Ma. The REE and trace element pattern of one of the P-rich patches in the garnet core is different from the P-rich garnet rim. The isotope mapping of the same patch by LA-ICPMS revealed that the patch is also observed as a domain depleted in ^{51}V, ^{89}Y, ^{165}Ho, ^{166}Er, ^{169}Tm, ^{172}Yb, and ^{175}Lu. Clear difference in ^{51}V concentration between the patch and the garnet rim suggests that this patch is not a continuous part from the garnet rim, but is likely a relic of preexisted garnet. Kyanite included in the patch suggests that the precursor rock was presumably a medium- to high-pressure type metamorphic rock. Presence of the older age population (~ 650-580 Ma) monazites in Skallevikshalsen and Skallen also suggest that rocks in these areas experienced polymetamorphism, and resetting by the ~ 560-500 Ma metamorphic event was incomplete in these areas. Taking into account the presence of Cl-rich biotite inclusions in garnet, infiltration of brine accompanied by partial melting is one probable event that took place at ~ 560-500 Ma in the Skallevikshalsen area, and part of the monazite possibly recrystallized by this brine infiltration.

Detailed microstructural observation using trace element mapping combined with detailed petrography especially focusing on the Cl-bearing minerals as a tracer of brines would become a powerful tool for better interpreting the results of monazite and zircon dating and for investigating the fluid-related crustal processes.

Keywords: Monazite, Zircon, Partial melting, Brine, Polymetamorphism

INTRODUCTION

Estimating the timing and duration of high-grade metamorphism through zircon and monazite dating can potentially place a very important constraint on the tectonic framework of lower crustal processes during continental collision events (e.g., Johnson and Harley, 2012; Rubatto et al., 2013; Korhonen et al., 2013). Recent advance in understanding the growth/recrystallization timing of zircon and monazite during metamorphic cycle, especially the roles of partial melting and fluid infiltration events in formation/dissolution/recrystallization of these minerals enable to reconstruct the lower crustal evolution in more detail (e.g., Rubatto et al. 2001; Rubatto, 2002; Harley and Kelly, 2007; Rubatto et al., 2013; Kawakami et al., 2013; 2014; Korhonen et al., 2013; Harley and Nandakumar, 2014).

Increasing number of natural examples of chloride brines show that its generation and migration are important geologic processes in the lower crust, in addition to the CO_2-rich fluid (Newton and Manning, 2010; Touret

and Huizenga, 2011; Smit and Van Reenen 1997; Markl and Bucher, 1998; Newton et al. 1998; Van den Berg and Huizenga 2001; Kullerud, 1995; Harlov and Forster, 2002; Rubenach, 2005; Higashino et al., 2013, 2015). Under the granulite facies conditions, chloride brine and CO_2-rich fluid can immiscibly coexist over a wide range of pressure (P) and temperature (T) conditions (Trommsdorff et al., 1985; Shmulovich and Graham, 1999, 2004; Heinrich, 2007). Chloride brines work as a powerful solvent for various minerals (Newton and Manning, 2010) and potentially can play an important role in mass transfer even without partial melting.

Minerals such as biotite, hornblende, apatite and scapolite can incorporate Cl in their crystal structure. Among these minerals, biotite and apatite are often used to estimate the f_{H_2O}/f_{HCl} ratio of the coexisting aqueous fluid (Munoz and Swenson, 1981; Selby and Nesbitt, 2000; Piccoli and Candela, 1994), although apatite is sometimes considered inert against fluid-related processes (Piccoli and Candela, 1994). The merit in using the Cl-bearing minerals as an indicator of the chloride brine activity is that the P-T path of the lower crustal granulite facies rocks can be better correlated with the timing of the brine existence, utilizing the microstructure of the Cl-bearing minerals (e.g., Satish-Kumar et al., 2006; Higashino et al., 2013).

In order to link the presence of Cl-rich hydrous minerals to the fluid-related events and partial melting in the lower continental crust, however, it is important to understand the formation processes of those minerals, especially in the presence of melt. However, limited number of experimental study on Cl partitioning is available only at low pressure conditions (e.g., Icenhower and London, 1997; Chevychelov et al., 2008). Icenhower and London (1997) determined the distribution coefficient of Cl between biotite and granitic melt to be 1-6 at 0.20 GPa and 640-680 °C. On the other hand, experiments at 0.20 GPa and ~ 850 °C showed that order of the Cl distribution is fluid ≫ phonolite melt > biotite (Chevychelov et al., 2008). Since experimental study and natural examples are still scarce under lower crustal conditions, more information on the mode of occurrence and chemistry of Cl-rich hydrous minerals in natural examples that experienced partial melting is needed in order to understand the partitioning behavior of Cl between hydrous minerals and melt, and the formation conditions of Cl-rich hydrous minerals in the lower crust. Detailed study of such natural example has an advantage because behavior of zircon and monazite can be examined and correlated with the possible Cl-bearing fluid (brine) infiltration and melt formation/crystallization.

In this study, mode of occurrence of Cl-rich biotite and apatite, together with important datable accessory minerals zircon and monazite in the garnet-sillimanite gneiss from Skallevikshalsen, Lützow-Holm Complex (LHC), East Antarctica is reported in detail. The mechanism of Cl-rich biotite and apatite formation and possible link between dissolution/formation/recrystallization of zircon and monazite is also discussed. Mineral abbreviations are after Kretz (1983).

GEOLOGY OF SKALLEVIKSHALSEN, LÜTZOW-HOLM COMPLEX, EAST ANTARCTICA

The LHC is a Cambrian orogenic belt bounded by the Late Proterozoic to Cambrian Rayner Complex to the east and by the Late Proterozoic to Early Palaeozoic Yamato-Belgica Complex to the west (Shiraishi et al., 1994). For the detailed geology of the surrounding Complexes, see Satish-Kumar et al. (2008a). Metamorphic grade of the complex progressively changes from upper amphibolite facies on the Prince Olav Coast to granulite facies in the Lützow-Holm Bay (Hiroi et al., 1991; Kawakami et al., 2006; 2008) (Fig. 1). A 'thermal axis' of maximum peak temperature is estimated to lie at the southern Lützow-Holm Bay, around Rundvågshetta (Motoyoshi and Ishikawa, 1997). Ultrahigh-temperature (*UHT*) metamorphism of about 1000 °C, 1.1 GPa and subsequent isothermal decompression are reported from Rundvågshetta (Kawasaki et al., 1993; Ishikawa et al., 1994; Yoshimura et al., 2008). The complex is deduced to have experienced a typical clockwise P-T path (Hiroi et al., 1983a, 1983b; 1986; Kawakami and Motoyoshi, 2004; Kawakami and Hokada, 2010). The rocks in the Prince Olav Coast experienced the reaction staurolite = garnet + Al_2SiO_5 + spinel + H_2O in the sillimanite stability field whereas those in the Lützow-Holm Bay experienced the reaction in the kyanite stability field (Hiroi et al., 1983a, 1983b, 1991).

Skallevikshalsen is about 30 km northeast of Rundvågshetta (Fig. 1), and is underlain by garnet-biotite gneiss, garnet-sillimanite gneiss, orthopyroxene-hornblende gneiss, garnet-two pyroxene gneiss, marble, skarn, and subordinate amount of discordant granitic pegmatites (Yoshida et al., 1976). At least, two ductile deformation events can be recognized from the fold interference patterns (Kawakami and Ikeda, 2004). The garnet-two pyroxene gneiss is commonly boudinaged, and leucosome is developed at the boudin necks between and within the granulite lens, indicating the occurrence of partial melting (Kawakami and Motoyoshi, 2004). Yoshimura et al. (2004) considered that the garnet-sillimanite gneiss is likely a restitic product of partial melting. Partial melting of the garnet-sillimanite gneiss is also supported by the presence of 'nanogranite' (Cesare et al., 2009) or 'felsite'
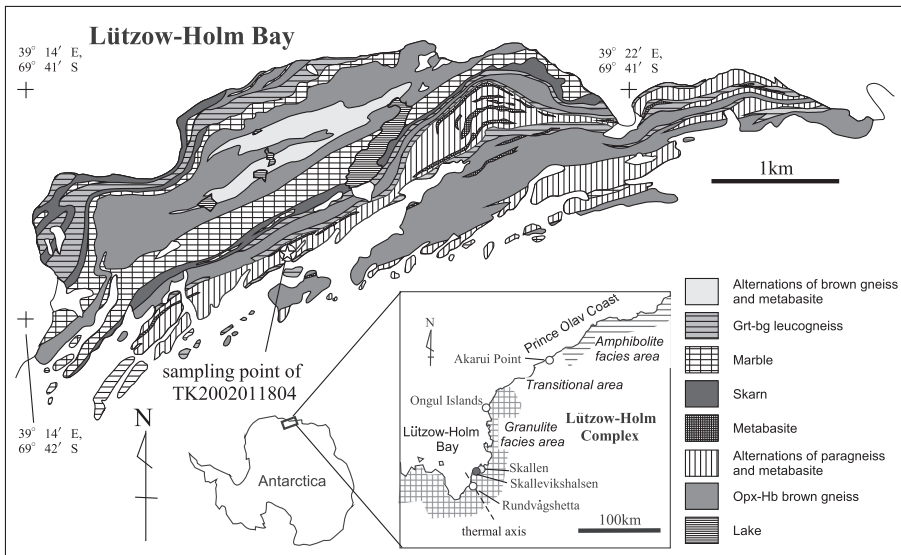
Figure 1. Geological map of Skallevikshalsen (after Yoshida et al., 1976) showing the sample locality of TK2002011804, and a simplified metamorphic zone map of the Lützow-Holm Complex (Hiroi et al., 1991).

(Hiroi et al., 2014) inclusions in garnet porphyroblasts (Kawakami and Hokada, 2010 and this study). Peak metamorphic condition of Skallevikshalsen was previously estimated to be 770–940 °C, 0.65–1.2 GPa from the garnet-biotite gneiss and 780–960 °C, 0.60–1.1 GPa from the garnet-two pyroxene gneiss (Yoshimura et al., 2004). The *UHT* condition exceeding 1000 °C was recently proposed, based on the occurrence of possible armalcolite pseudomorph (Kawasaki et al., 2013).

Previous SHRIMP ages from zircon separates concentrate around 550–530 Ma, and were interpreted as timing of peak metamorphism in the LHC (e.g., Shiraishi et al., 1994). However, from the in situ SHRIMP analyses of zircon inclusions in garnet porphyroblasts, Dunkley (2007) revealed a stage of U-rich zircon growth at ~ 600 Ma, with flat HREE-MREE profiles indicating prograde growth in the presence of garnet (Dunkley, 2007). Therefore, ~ 600–570 Ma is considered to be the timing of prograde to peak metamorphism, and 550–530 Ma to be the retrograde zircon growth stage (Dunkley, 2007). Kato (2013) dated zircon from syenite dyke and associated charnockite that postdate the peak metamorphism at Skallevikshalsen, and obtained the age of 550–530 Ma. This is also consistent with the peak metamorphism and penetrative deformation in the Skallevikshalsen area to be earlier than 550–530 Ma (Kato, 2013).

ANALYTICAL METHODS

The X-ray mapping of the garnet grains were obtained by a JEOL JXA8800M at the National Institute of Polar Research (NIPR) and by a JEOL superprobe JXA-8105 at Kyoto University. Analytical conditions for X-ray mapping were 15.0 kV acceleration voltage, 400–800 nA probe current with focused beam to defocused beam up to 5 μm diameter. Minerals were quantitatively analyzed by the JEOL superprobe JXA-8105 at Kyoto University. Analytical conditions were 15.0 kV acceleration voltage, 10 nA probe current with probe diameter of 3 μm. The counting time for the peak and backgrounds were 30 s and 15 s for Cl, 60 s and 30 s for F, and 10 s and 5 s for other elements, respectively. Natural and synthetic minerals were used for standards, and ZAF correction was applied. Analytical condition of rutile for Zr-in-rutile geothermometry followed that recommended by Zack et al. (2004). Counting error was about ±2% for Zr, which yielded ignorable small (±2°C) variation in the result of Zr-in-rutile geothermometry. Al_2SiO_5 minerals and fluid inclusions were identified by Raman spectroscopy at NIPR (JASCO NRS 1000) and Kyoto University (JASCO NRS 3100).

The electron microprobe (EMP) dating and REE analyses of monazite were carried out using a JEOL JXA-8200 at NIPR. Detailed analytical technique is given in Hokada and Motoyoshi (2006).

In situ laser ablation inductively coupled plasma mass spectrometry (LA-ICPMS) analyses of rare earth elements (REE) and trace element concentrations of garnet were performed using an iCAP-Qc quadrupole ICPMS coupled to a NWR-193 laser-ablation system at Kyoto University. Detailed analytical conditions are reported in Higashino et al. (2015). In situ isotope mapping on a thin section sample was performed using the same system. Data processing was done using a software *iQuant2*. Analytical conditions are given in Table S1 (Tables S1 is available online from http://doi.org/10.2465/jmps.150812).

In situ zircon U-Pb dating on thin section samples by LA-ICPMS was carried out using a Nu Plasma II HR-

MC-ICPMS coupled with a NWR-193 laser-ablation system at Kyoto University. Analytical conditions are given in Table S2 (Tables S2 is available online from http://doi.org/10.2465/jmps.150812). Backscattered electron (BSE) and cathodoluminescence (CL) images were obtained prior to the analyses to identify spot positions, overlapping multiple growth zones, grain edges, cracks or damaged zircon grains. Data were processed and plotted using *Isoplot 4.15* (Ludwig, 2012). The CL images were obtained using a JEOL JXA-8105 superprobe equipped with Hamamatsu Photonics high voltage power supply C9525 and photon counting unit C9744 at Kyoto University. Analytical condition for the CL mapping of zircon was 15.0 kV acceleration voltage, 1 nA beam current, focused beam, and dwell time of 1 milliseconds.

SAMPLE DESCRIPTION

The sample used in this study is a khondalitic garnet-sillimanite gneiss (sample TK2002011804) collected during the summer season of the 44th Japan Antarctic Research Expedition (JARE44; 2002-2003). The sample mainly consists of garnet (~ 5 mm in diameter), sillimanite, K-feldspar, plagioclase and quartz with minor biotite, rutile, ilmenite, zircon, monazite and pyrite (Kawakami and Motoyoshi, 2004; Kawakami et al., 2006; Kawakami and Hokada, 2010). It is noteworthy that the rock matrix contains no hydrous mineral except for minor amount of biotite. Apatite is very rare in the rock matrix. This sample has an advantage of including many relic inclusions indicative of *P-T* path in the garnet porphyroblasts (Kawakami and Motoyoshi, 2004; Kawakami and Hokada, 2010). In this study, garnet grains A, B, C and E of Kawakami and Hokada (2010) are studied in detail (Figs. 2-5). Garnets A and C are from the thin section TK2002011804d, and garnets B and D are from the thin section TK2002011804c.

The garnet grains have sharp zoning in phosphorus, and can be divided into P-poor core (20-60 ppm, determined by LA-ICPMS in the present study) and P-rich rim (70-140 ppm). The garnet core includes biotite, staurolite, kyanite, kyanite + spinel + biotite (presumably after staurolite), prismatic sillimanite, spinel + quartz, plagioclase (An43-45 at the inner core, An15 and An5 at the outer core), quartz, rutile, zircon, apatite and fine-grained monazite (<52 μm; Kawakami and Hokada, 2010) (Figs. 2-5). Prismatic sillimanite is only rarely included in the outermost core of the garnet. Chlorine-rich biotite (>0.3 wt%Cl, up to 0.41 wt%Cl) is exclusively included in the garnet core (Figs. 2-5; Table 1). Fluorine content in biotite is also high (up to 0.60 wt%F). In most cases, Cl-rich biotite is also rich in TiO_2 (4.4-6.3 wt%). Nanogranite

inclusions (Cesare et al., 2009) or felsite inclusions (Hiroi et al., 2014) are exclusively included in the garnet core and are not found in the garnet rim. The mineral assemblage of the nanogranite/felsite inclusion varies, and muscovite + quartz + chlorite intergrowth was previously reported (Kawakami and Hokada, 2010). Another example of a large nanogranite/felsite inclusion that consists of intergrowth of plagioclase (An26-28) + K-feldspar + quartz + muscovite + minor biotite (Fig. 6a) is newly found in this study. Muscovite and chlorite are formed between the intergrowth and host garnet, and cuspate or spear-shaped replacement by muscovite is developed from the edges of the nanogranite/felsite inclusion into the host garnet (e.g., Hiroi et al., 2014). Post entrapment chemical re-equilibrium between host garnet and nanogranite/felsite inclusion is inferred from the halo of Fe and Mg developed around the inclusion (Fig. 6a). Chlorine content of biotite in the intergrowth is lower than that included in garnet as a single mineral. Finer-grained nanogranite/felsite inclusions with the cuspate or spear-shaped replacement microstructure are abundantly included in the garnet core without any internal alignment (Figs. 6b-6c). Apatite included in the garnet core is mostly Cl-bearing fluorapatite (up to 1.88 wt%Cl, 0.26 a.p.f.u. under O = 12.5, n=18) (Table 1).

On the other hand, the garnet rim includes sillimanite needles, plagioclase, K-feldspar, quartz, zircon and coarse-grained monazite (<147 μm). K-feldspar is included in the rim or at the boundary between the core and the rim (Kawakami and Hokada, 2010).

Matrix biotite shows lower Cl contents (0.06-0.13 wt%Cl) than the inclusion biotite. TiO_2 content varies from 2.0 to 4.9 wt% with one exception of 6.0 wt%, the average being 3.8 wt% (n = 14) (Table 1). Rare matrix apatite is fluorapatite, and its Cl content is below detection limit (n = 1) (Table 1).

Trace element and REE analyses by LA-ICPMS revealed that garnet core is lower in P and Cr, and higher in HREE contents than the rim (Fig. 7 and Table 2: Table 2 is available online from http://doi.org/10.2465/jmps. 150812). P-rich patches are present in garnet cores as revealed by EMP mapping (Figs. 2 and 5; Kawakami and Hokada, 2010). Two of these patches are analyzed quantitatively for trace elements and REE. As a result, one patch from garnet E (Fig. 5) showed similar trace element and REE composition with the garnet rim, and the other patch from garnet A (Fig. 2) showed lower Cr and higher Y and HREE concentrations than the rim (Fig. 7). In situ isotope mapping of this P-rich patch from garnet A by LA-ICPMS revealed that it is also observed as a domain depleted in ^{51}V, ^{89}Y, ^{165}Ho, ^{166}Er, ^{169}Tm, ^{172}Yb, and ^{175}Lu (Fig. 2).
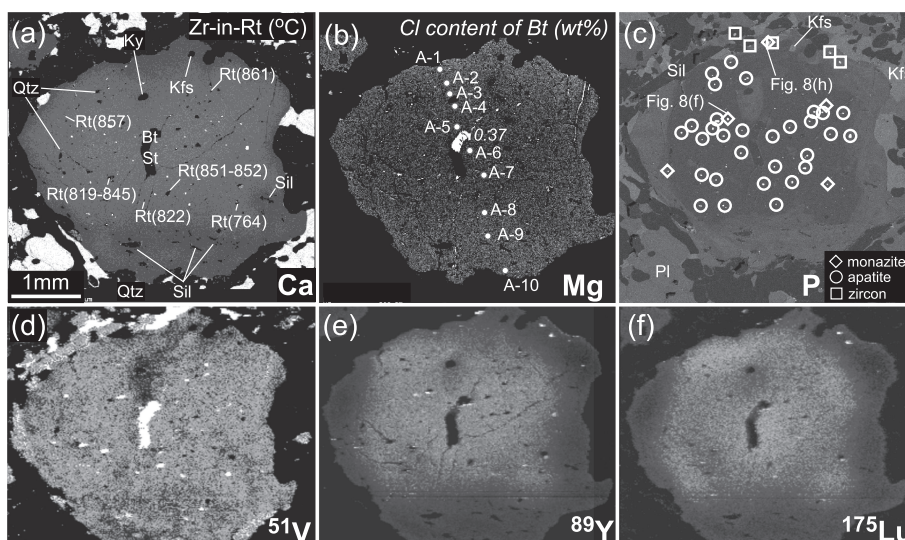
Figure 2. (a) X-ray elemental map of 'garnet A' in terms of Ca, with information of mineral inclusions and the results of the Zr–in–rutile thermometry (Tomkins et al., 2007) for inclusion rutile. Some of the abundant tiny-grained inclusions in the garnet core are the multi-phase inclusions with cuspate or spear-shaped replacements that presumably share the same origin as nanogranite/felsite inclusions. (b) X-ray elemental map of the garnet A in terms of Mg, with Cl concentrations of inclusion biotite grains (white grains). A-1 to A-10 are the points where the LA-ICPMS analyses of trace elements and REE were performed. (c) X-ray elemental map of the garnet A in terms of P, showing the sharp zoning of P in the garnet and locations of monazite grains dated by EMP. (d) Isotope mapping by the LA-ICPMS in terms of ^{51}V. Note the low ^{51}V patch just above the staurolite inclusion corresponds with P-rich patch in (c). (e) Isotope mapping by the LA-ICPMS in terms of ^{89}Y. (f) Isotope mapping by the LA-ICPMS in terms of ^{175}Lu.
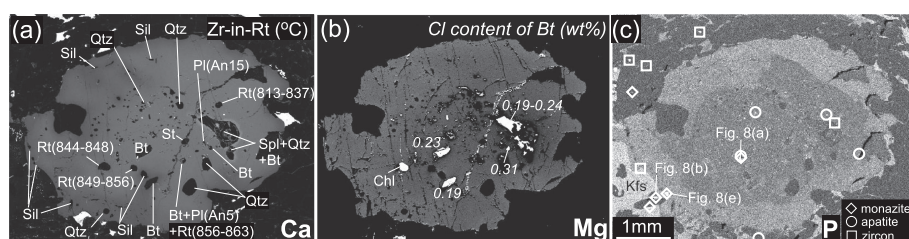
Figure 3. (a)–(c) X-ray elemental map of 'garnet B'. Other details are the same as Figures 2a-2c.

## ZIRCONIUM-IN-RUTILE GEOTHERMOMETRY

Zr–in–rutile geothermometer (Zack et al., 2004; Ferry and Watson, 2007; Tomkins et al., 2007) was applied to rutile crystals included in the garnets A, B, C and E. Rutile inclusions are not accompanied with zircon or quartz, and these minerals are separately included in the core of garnet porphyroblasts. Rutile grains coexisting with ilmenite are not used, because activity of TiO_2 may be lower than unity and difficult to estimate. Zr–in–rutile geothermometer by Zack et al. (2004) gave 960–1025 °C for most grains. The result by Tomkins et al. (2007) is preferred in this study because it is experimentally calibrated and pressure effect is taken into account. Zr–in–rutile geothermometer by Ferry and Watson (2007) gave slightly lower (~ 10 °C) temperature estimate than Tomkins et al. (2007), suggesting the reliability of the estimated values.

　Most of the grains gave Zr concentration of ~ 2200–3300 ppm, with the average of ~ 2560 ppm (n = 43, av-

eraged excluding the data below 1200 ppm). Under the coexistence of kyanite, and using the Al_2SiO_5 triple point and Sil/Ky transition of Pattison (1992), these values corresponds to pressures above ~ 1.1 GPa and temperatures above ~ 840 °C. In Figures 2–5, temperature value calculated using the pressure of 1.2 GPa is shown. Some rutile grains included together with other minerals, such as plagioclase or biotite + staurolite + kyanite + spinel, gave lower temperature estimates. In the latter case, biotite coexisting with rutile showed apparently lower Cl content than other biotite grains included independently in the same garnet grain (Fig. 5b). A rutile grain included in garnet together with plagioclase (An43-45) gave 795–802 °C.

EMP MONAZITE DATING

The monazite grains dated in situ by EMP are from the rock matrix (3 grains), included in the garnet core (5 grains including one grain at the core/rim boundary),
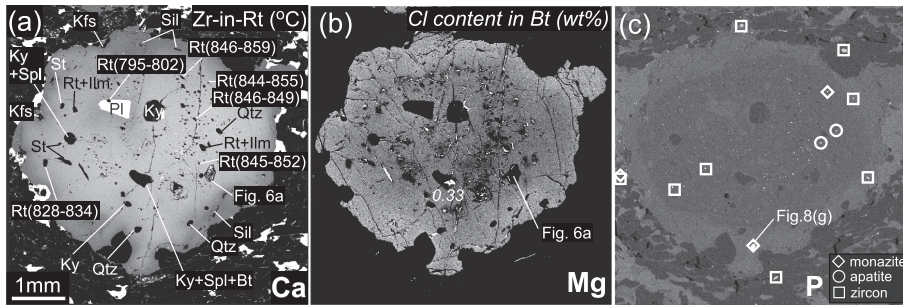
Figure 4. (a)-(c) X-ray elemental map of 'garnet C'. Other details are the same as Figures 2a-2c.
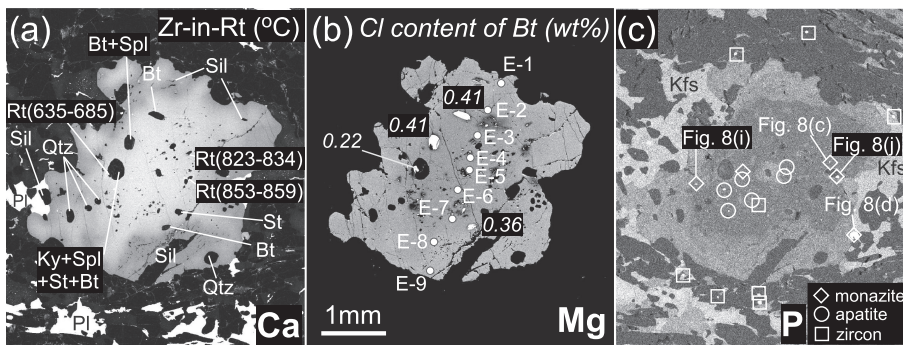
Figure 5. (a)-(c) X-ray elemental map of 'garnet E'. E-1 to E-9 are the points where the LA-ICPMS analyses of trace elements and REE were performed. Other details are the same as Figures 2a-2c.

or included in the garnet rim (2 grains). Inclusion monazite grains dated are from garnets A, B, C and E described in Kawakami and Hokada (2010).

Back-scattered electron image of monazite grains and result of EMP monazite dating are summarized in Figure 8, and the analytical results are reported in Table S3 (Tables S3 is available online from http://doi.org/10.2465/jmps.150812). Y_2O_3 was accidentally not analyzed. Five grains that occur as garnet inclusion and matrix phase yielded weighted average age (±2σ error) of 564 ± 42 Ma (n = 5, MSWD = 0.42), 549 ± 11 Ma (n = 42, MSWD = 0.28), 538 ± 31 Ma (n = 9, MSWD = 0.11), 520 ± 28 Ma (n = 9, MSWD = 0.26), and 516 ± 27 Ma (n = 7, MSWD = 0.45). On the other hand, one grain included at the rim of garnet C yielded weighted mean age of 604 ± 13 Ma (n = 34, MSWD = 0.29). Other grains did not give sufficient number of analyses to calculate the weighted mean age from a single grain. Compared to the monazite with older age (604 ± 13 Ma), the grains with younger ages tend to be lower in MREE and U concentration, and higher in Th concentration and Th/U ratio (18-73) (Fig. 9; Table S3).

LA-ICPMS U-PB ZIRCON DATING

Zircon grains dated in situ by the LA-ICPMS are mostly from the matrix (n = 15, major axis = 24-104 μm), and 4 grains are included in garnet (major axis = 15-50 μm). Most of the zircon grains are zoned, and tend to have inherited cores showing oscillatory zoning with bright and dark CL zones (Figs. 10a-10d). It is commonly overgrown by gray to dark CL rims (Figs. 10a-10d).

Inherited cores commonly yield discordant data (Figs. 10a-10c and 10e). On the other hand, zircon rims commonly yield concordant data (Figs. 10a, 10c-10d, and 10f). Gray to dark CL rims of the matrix zircon tend to show $^{206}Pb/^{238}U$ ages of ~ 530-510 Ma (Figs. 10a and 10c; Table 3: Table 3 is available online from http://doi.org/10.2465/jmps.150812). Rim of one zircon inclusion in garnet and some of the matrix zircon rims show $^{206}Pb/^{238}U$ ages of ~ 595-580 Ma (Fig. 10d). Zircon domain with ~ 530-510 Ma is not found as garnet inclusions in the studied sample. Zircon domains with ~ 530-510 Ma age tend to show higher Th, lower U contents and slightly higher Th/U ratio (0.02-0.30) than those with ~ 595-580 Ma age (0.01-0.10). A concordia diagram of all analyses and the probability density plot constructed for the concordant data are shown in Figures 10e-10g. Age unmixing based on the algorithm of Sambridge and Compston (1994) assuming two components for concordant zircon rim ages yielded 595 ± 11 Ma and 524 ± 7 Ma (Fig. 10g).

DISCUSSION

Pressure-temperature condition of Cl-rich biotite formation

Since the homogenization of rutile grain in terms of Zr content during high-temperature metamorphism cannot be ruled out, the highest temperature estimate obtained from the Zr-in-rutile thermometer should be considered as representing the minimum temperature attained. Therefore, the temperature estimate of 820-850 °C obtained

Table 1. Representative electron microprobe analyses of biotite and apatite

| Sample no.	TK200201 1804c	TK200201 1804d	TK200201 1804c	TK200201 1804c	TK200201 1804c	TK200201 1804d	TK200201 1804d	TK200201 1804d	TK200201 1804c	TK200201 1804c	TK200201 1804c
Mineral	Bt	Bt	Bt	Bt	Bt	Bt	Bt	Apt	Apt	Apt	Apt
Mode of occurrence	Inclusion in GrtB	Inclusion in GrtC	Inclusion in GrtE	Inclusion in GrtE	GrtE[*4]	In matrix	Matrix Bt	Inclusion in GrtA	Inclusion in GrtB	Inclusion in GrtE	Matrix near GrtB
Analysis no.	Cl15	Cl24	Cl1	25F (NIPR)[*3]	Cl5	804d-bt0706-1	804d-bt0706-6	GrtA-5	GrtB-1	GrtE-4	GrtB-2
SiO_2	37.33	36.68	36.72	37.09	36.91	36.74	36.80	0.12	0.10	0.13	0.43
TiO_2	0.40	6.28	6.14	4.50	2.09	3.83	5.97	0.11	0.02	0.00	0.00
Al_2O_3	22.27	16.06	17.05	16.70	19.56	16.53	15.99	0.09	0.03	0.01	0.29
Cr_2O_3	0.00	0.02	0.10	0.06	0.01	0.12	0.05	n.d.	n.d.	n.d.	n.d.
FeO	9.93	14.97	11.73	12.72	10.14	11.21	13.99	1.31	0.92	0.87	0.12
ZnO	n.d.	n.d.	n.d.	0.06	n.d.	n.d.	n.d.	n.d.	n.d.	n.d.	n.d.
MnO	0.00	0.00	0.12	0.00	0.00	0.06	0.00	0.01	0.00	0.08	0.00
MgO	15.54	12.46	13.82	13.98	17.34	15.70	13.27	0.14	0.06	0.01	0.01
CaO	0.00	0.00	0.00	0.00	0.03	0.00	0.02	54.08	54.75	54.84	54.71
BaO	0.25	0.70	0.68	n.d.	0.07	0.20	0.21	0.00	0.00	0.23	0.00
Na_2O	0.20	0.10	0.18	0.16	0.11	0.11	0.07	0.03	0.00	0.10	0.00
K_2O	9.04	8.96	9.16	9.66	8.55	9.77	9.61	0.00	0.02	0.02	0.28
P_2O_5	n.d.	n.d.	n.d.	n.d.	n.d.	n.d.	n.d.	43.12	43.61	42.88	44.33
F	0.09	0.16	0.26	0.43	0.14	0.28	0.36	2.41	2.09	1.98	3.40
Cl	0.31	0.33	0.36	0.41	0.19	0.12	0.13	1.05	1.79	1.64	0.01
$-O \equiv F$	0.04	0.07	0.11	0.18	0.06	0.12	0.15	1.01	0.88	0.83	1.43
$-O \equiv Cl$	0.07	0.07	0.08	0.09	0.04	0.03	0.03	0.24	0.40	0.37	0.00
Total	95.25	96.57	96.13	95.50	95.02	94.51	96.28	101.22	102.11	101.56	102.13
Number of O	22	22	22	22	22	22	22	12.5	12.5	12.5	12.5
Si	5.40	5.44	5.40	5.50	5.36	5.47	5.44	0.01	0.01	0.01	0.03
Ti	0.04	0.70	0.68	0.50	0.23	0.43	0.66	0.01	0.00	0.00	0.00
Al	3.79	2.81	2.95	2.92	3.35	2.90	2.79	0.01	0.00	0.00	0.03
Cr	0.00	0.00	0.01	0.01	0.00	0.01	0.01	n.d.	n.d.	n.d.	n.d.
Fe	1.20	1.86	1.44	1.58	1.23	1.40	1.73	0.09	0.06	0.06	0.01
Mn	0.00	0.00	0.01	0.00	0.00	0.01	0.00	0.00	0.00	0.01	0.00
Mg	3.35	2.75	3.03	3.09	3.75	3.48	2.93	0.02	0.01	0.00	0.00
Ca	0.00	0.00	0.00	0.00	0.00	0.00	0.00	4.79	4.82	4.87	4.75
Ba	0.01	0.04	0.04	0.00	0.00	0.01	0.01	0.00	0.00	0.01	0.00
Zn	n.d.	n.d.	n.d.	0.01	n.d.	n.d.	n.d.	n.d.	n.d.	n.d.	n.d.
Na	0.06	0.03	0.05	0.04	0.03	0.03	0.02	0.01	0.00	0.02	0.00
K	1.67	1.70	1.72	1.83	1.58	1.85	1.81	0.00	0.00	0.00	0.03
P	n.d.	n.d.	n.d.	n.d.	n.d.	n.d.	n.d.	3.02	3.03	3.01	3.04
F	0.04	0.07	0.12	0.20	0.06	0.13	0.17	0.63	0.54	0.52	0.87
Cl	0.08	0.08	0.09	0.10	0.05	0.03	0.03	0.15	0.25	0.23	0.00
Total cation	15.52	15.32	15.33	15.47	15.55	15.59	15.41	7.95	7.94	7.98	7.90
$Mg/(Fe_{total}+Mg)$	0.74	0.60	0.68	0.66	0.75	0.71	0.63	0.16	0.10	0.20	0.11
$\log(f_{H2O}/f_{HCl})$ of fluid [*1]	3.78	3.35	3.33	3.24	3.68	n.d.	n.d.	2.16	1.90	2.02	4.10
$\log(f_{H2O}/f_{HF})$ of fluid [*1]	4.93	4.52	4.37	4.12	4.76	n.d.	n.d.	4.41	4.45	4.55	4.03
Temperature (°C) [*2]	850	850	850	850	850	n.d.	n.d.	850	850	850	850

[*1] Based on Munoz (1992) for biotite, and Piccoli and Candela (1994) for apatite.

[*2] Temperature used in calculating $\log(f_{H2O}/f_{HCl})$ of the fluid coexisted with biotite and/or apatite. Temperature estimate is based on Zr-in-rutile thermometer. See text for details.

[*3] Analyzed in NIPR. See Kawakami and Motoyoshi (2004) for analytical conditions.

[*4] In nanogranite-like inclusion in GrtE.

n.d., not determined.
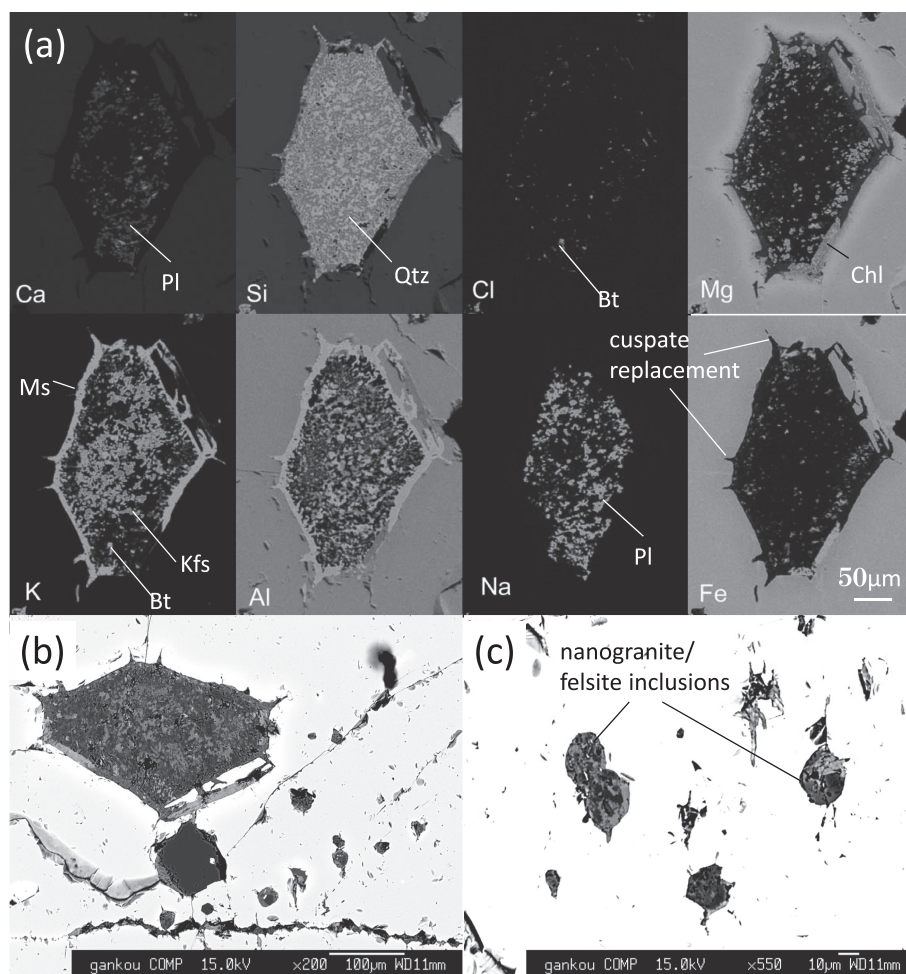
Figure 6. (a) X-ray elemental maps of a nanogranite/felsite inclusion in the garnet C (Fig. 4), in terms of Ca, Si, Cl, Mg, K, Al, Na and Fe. Biotite (Bt), muscovite (Ms), K-feldspar (Kfs), quartz (Qtz), plagioclase (Pl) and chlorite (Chl) are shown. (b) Back scattered electron (BSE) image of the garnet core containing the nanogranite/felsite inclusion shown in (a). Fine-grained nanogranite/felsite inclusions are also included in the garnet core. (c) Enlargement of fine-grained nanogranite/felsite inclusions in the garnet core. BSE image. Color version of Figure 6 is available online from http://doi.org/10.2465/jmps.150812.

from the rutile included in the garnet core is regarded as minimum temperature for the garnet core formation. Thus, Cl-rich biotite and kyanite included in the garnet core were stable under pressures >1.2 GPa and temperatures >850 °C, and coexisted with granitic melt as suggested by the presence of nanogranite/felsite inclusion in the garnet core (Fig. 6). Peak metamorphic temperature of 848 ± 55 °C reported from Skallen (Satish-Kumar and Wada, 2000) adjacent to Skallevikshalsen is quite similar to our temperature estimate. Kawasaki et al. (2013) also reported the temperature estimate by Zr-in-rutile thermometer, which gave mostly consistent results with this study. The pressure condition under the kyanite stability field is previously estimated to be slightly lower than 1.2 GPa (e.g., Yoshimura et al., 2004; Kawakami and Motoyoshi, 2004), because of the lower-temperature estimate than the present study.

Formation mechanism of Cl-enriched biotite included in garnet

Chlorine-rich biotite is exclusively preserved as inclu-

sions in garnet (Figs. 2-5), suggesting prograde to peak metamorphic origin. Therefore, the process such as retrograde formation of biotite to preferentially consume H_2O in the fluid phase, resulting in the increase of the Cl concentration in the remaining fluid (e.g., Markl and Bucher, 1998) is not likely in the present case. Instead, partial melting process is clearly related to the present case, because the nanogranite/felsite inclusions coexist with Cl-rich biotite in the garnet core (Fig. 6). In addition, the nanogranite/felsite inclusions are not found in the garnet rim, and not always aligned (Figs. 6b-6c). These suggest that the melt, now observed as nanogranite/felsite inclusions, was captured during the stages of the garnet core growth and between the garnet core and rim growths, and the nanogranite/felsite inclusions do not represent the melt that infiltrated after the garnet rim growth. Progress of continuous dehydration melting of biotite to form peritectic garnet would increase the Cl concentration in biotite by consuming originally Cl-poorer biotite, if Cl is preferentially incorporated into biotite. Scarcity of the matrix biotite, in spite of the common occurrence of bio-

(a)

(b)

(c)
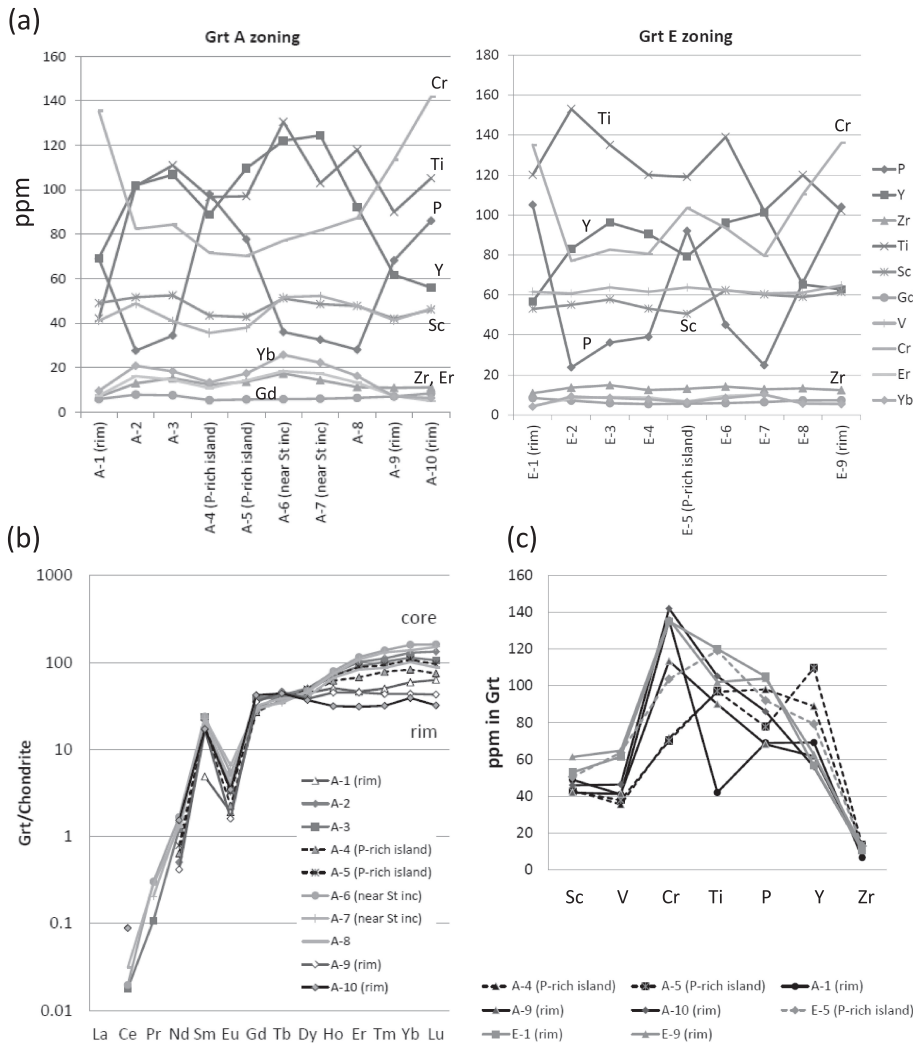
Figure 7. Trace element and REE analyses of garnet by the LA-ICPMS. (a) Line traverse analysis of the garnets A and E. Both have P-rich patches. (b) Chondrite-normalized REE pattern of the garnet A composition. Note that the rim compositions and the P-rich patch compositions are different. (c) Comparison of trace element composition between rims and P-rich patches of the garnets A and E. The P-rich patch in the garnet E shows similar pattern as the garnet E rim, whereas that in the garnet A shows different pattern from the garnet A rim. Color version of Figure 7 is available online from http://doi.org/10.2465/jmps.150812.

tite as inclusions in garnet, suggests almost complete consumption of pre-existed biotite during the prograde to peak metamorphism in the studied sample.

Experimental studies showed that partial melting triggered by the infiltration of H_2O fluid can also produce peritectic garnet (Weinberg and Hasalová, 2015). Therefore, the processes such as selective consumption of H_2O in the fluid into the melt to increase the Cl concentration in the remaining fluid, or the infiltration of already Cl-rich fluid, such as brines, to trigger partial melting (Aranovich et al., 2013), may also account for the presence of Cl-rich biotite coexisted with melt. High TiO_2 contents of the Cl-rich biotite inclusions in the garnet core support their formation during the prograde to peak metamorphism.

However, experimental study on the partitioning of Cl between biotite and melt is only available at low-pressure condition at 0.2 GPa (Icenhower and London, 1997; Chevychelov et al., 2008) and thus partitioning behavior of Cl in high-pressure condition is not well understood. On the other hand, partitioning of Cl between melt and

coexisting H_2O fluid is better constrained at higher-pressure up to 0.6 GPa (Shinohara et al., 1989; Piccoli and Candela, 1994), and a remarkable negative pressure dependence of D_{Cl}(melt/fluid) [= (Cl concentration in melt)/(Cl concentration in H_2O fluid)] is reported (Shinohara et al., 1989). Chlorine is significantly partitioned into fluid, if present, than the coexisting melt at higher pressures.

If we assume D_{Cl}(Bt/melt) of ~ 1 to 6 as observed in 0.2 GPa for a granitic melt (Icenhower and London, 1997) to be applicable to high-pressure conditions observed in the Skallevikshalsen sample, the melt coexisted with Cl-rich biotite (~ 0.40 wt%Cl; Table 1) should have 0.07 wt% < Cl < 0.40 wt%. On the other hand, apatite included in the garnet shows $XCl_{apatite}$ [= Cl/(Cl + F + OH)] of 0.12-0.25 (Table 1), corresponding to ~ 0.45-0.55 wt%Cl in the rhyolitic melt at 0.2 GPa (Webster et al., 2009). These are not unrealistic values for natural rhyolite melts. Therefore, keeping in mind that high-pressure behavior of Cl may be different from low-pressure as 0.2 GPa, we can tentatively consider that Cl-rich biotite and apatite in the studied
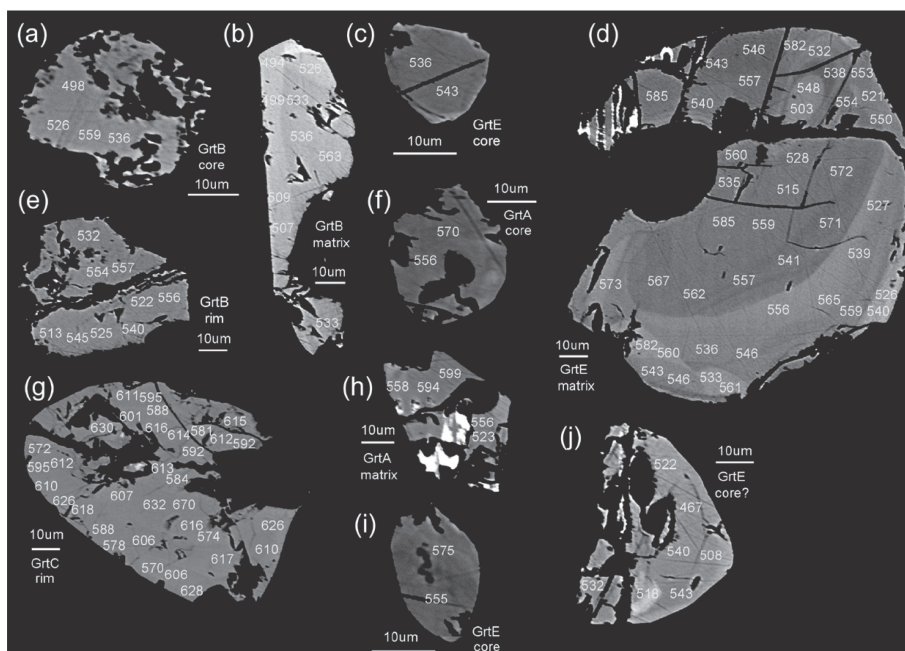
Figure 8. BSE images of monazite grains dated by the electron microprobe. Numbers in the BSE images are the apparent ages calculated assuming common Pb and inherited Pb to be zero. Grains (a), (c), (f) and (i) were not used for the calculation of weighted-mean ages.

sample would have coexist with melt, and were possibly produced through partial melting consuming biotite.

Whether external input of Cl is required to attain ~ 0.40 wt%Cl in biotite or not depends on initial Cl content in biotite and degree of partial melting that consumes biotite. However, in Skallen and Skallevikshalsen, Cl-rich scapolite in marbles has been considered as a result of hypersaline fluid that was present during scapolite formation (Satish-Kumar et al., 2006; 2008b). Since Cl-rich scapolite is stable under the peak *P-T* condition (>1.2 GPa, 820-850 °C) of Skallevikshalsen (e.g., Filiberto et al., 2014), infiltration of brine during prograde to peak metamorphic stage is highly likely (e.g., Satish-Kumar et al, 2008b). Therefore, brine infiltration into the pelitic lithology, followed by the partial melting process discussed above, is one of the possible processes to have elevated the Cl content in biotite in the studied sample. Source of such brine is still not understood, and should be solved in the future studies.

EMP monazite and LA-ICPMS U-Pb zircon ages

The EMP monazite ages of 604 ± 13 Ma and 564 ± 42 Ma to 516 ± 27 Ma obtained from this study corresponds well with two age populations of ~ 650-580 Ma and ~ 560-500 Ma previously reported from Skallen (Hokada and Motoyoshi, 2006) next to Skallevikshalsen (Fig. 1). The older ~ 650-580 Ma monazite from Skallen are reported to be relatively enriched in Nd, Sm, Gd, Dy (M-HREE) and depleted in Si, Ca and Th compared with the younger ones (Hokada and Motoyoshi, 2006). These chemical characteristics observed in these older and younger monazite populations are similar to those observed in Skallevikshalsen (Fig. 9).

The younger age population of monazite corresponds well with the ~ 550-520 Ma SHRIMP zircon age observed throughout the LHC (Shiraishi et al., 1994; 2008). In situ LA-ICPMS U-Pb zircon dating by this study (Fig. 10; Table 3) yielded two Neoproterozoic to Early Cambrian age populations, 595±11 Ma and 524±7 Ma, from zircon from Skallevikshalsen (Fig. 10g). These age populations correspond well with the older and younger age populations of monazite. Therefore, the term 'older age population' and 'younger age population' are used both for monazite and zircon hereafter to represent grains or domains yielding the ages of ~ 650-580 Ma and ~ 560-500 Ma. Chemical characteristics of the younger age population monazites, such as high Th/U ratio and high Th content than the older age population monazites, are also observed in zircon as well. That is, the younger age population zircons show the higher Th/U ratio of <0.30 and higher Th content than the older age population zircons (Table 3).

Hokada and Motoyoshi (2006) interpreted the older age population monazite to have grown in M-HREE rich condition such as garnet-free condition, and thus predated peak metamorphism. On the other hand, Dunkley (2007) revealed a stage of U-rich zircon growth at ~ 600 Ma (older age population zircons), with flat M-HREE profiles indicating prograde growth in the presence of garnet (Dunkley, 2007). He interpreted 550-530 Ma zircon (younger age population zircon) to be the retrograde product (Dunkley, 2007). It is also confirmed in the pres-

(a)

(b)

(c)
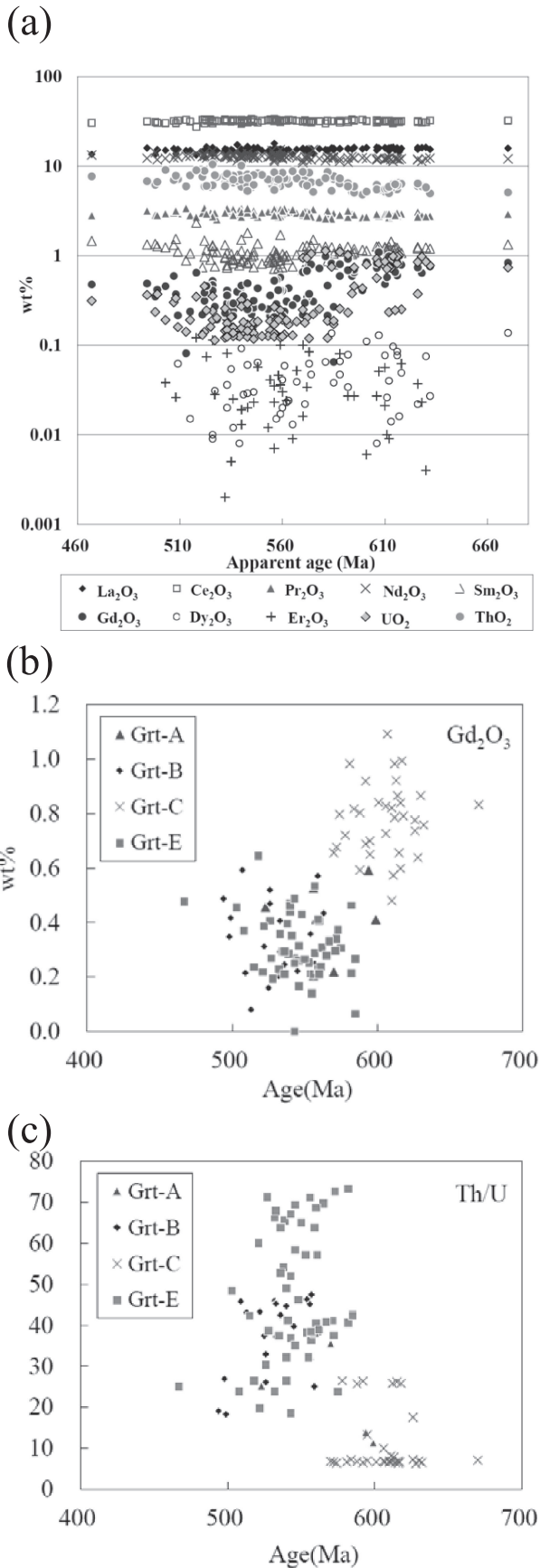
ent study that older age population zircon occur both as an inclusion in garnet and as the matrix phase, whereas younger age population zircons do not occur as inclusions in garnet. However, linking zircon growth stages using REE pattern needs caution, because under open-system condition, host-rock mineralogy such as the presence of garnet can have no chemical impact on zircon chemistry (Harley and Nandakumar, 2014). In order to account for the available observation, it is also possible to assume zircon growth timings in two separate metamorphic events; zircon growth at ~ 600 Ma metamorphism (older age population zircon) accompanied garnet growth, and that during 550–530 Ma metamorphism (younger age population zircon) postdated garnet growth. Since the presence of nanogranite/felsite inclusion in the garnet (Fig. 6) is a clear evidence of garnet coexisted with granitic melt, zircon probably experienced dissolution in the melt during the prograde garnet growth stage, and crystallized during the retrograde, melt crystallization stage.

Different from zircon, the younger age population monazites are included in garnet (Fig. 8). The chemical feature of the younger age population monazite having lower MREE concentrations than the older age population monazite (Fig. 9) is consistent with coexistence with garnet. This implies that garnet growth and most of the formation/recrystallization of the younger age population monazite predated recrystallization of zircon during the 550–530 Ma metamorphism. Therefore, it is likely that the older age population monazite recrystallized to form the younger age population monazite, possibly through the dissolution-reprecipitation mechanism, during the prograde to peak stage of metamorphism at 560–500 Ma under the presence of garnet and melt as suggested by the nanogranite/felsite inclusions in the monazite-bearing garnet. This was presumably followed by the zircon growth during the melt crystallization and partial resorption of garnet. Some of the young-aged monazite may be

Figure 9. (a) REE, Th and U in monazite as a function of apparent U–Th–Pb monazite ages determined by the EMP. Note that the older monazite has higher Gd_2O_3, Sm_2O_3, and UO_2 contents, and lower ThO_2 content than the younger monazite. (b) A plot showing the correlation between Gd_2O_3 contents in monazite and apparent U–Th–Pb monazite ages. Note that the older monazite is richer in Gd_2O_3. (c) A plot showing the correlation between the Th/U ratios of monazite vs apparent U–Th–Pb monazite ages. Note that the older monazite has low Th/U ratio. (b)–(c) 'Garnet A' represent monazite analyses from the grains (f) and (h) in Figure 8, 'Garnet B' represents those from the grains (a), (b), and (e), 'Garnet C' represents those from the grain (g), and 'Garnet E' represents those from the grains (c), (d), (i), and (j). Color version of Figure 9 is available online from http://doi.org/10.2465/jmps.150812.
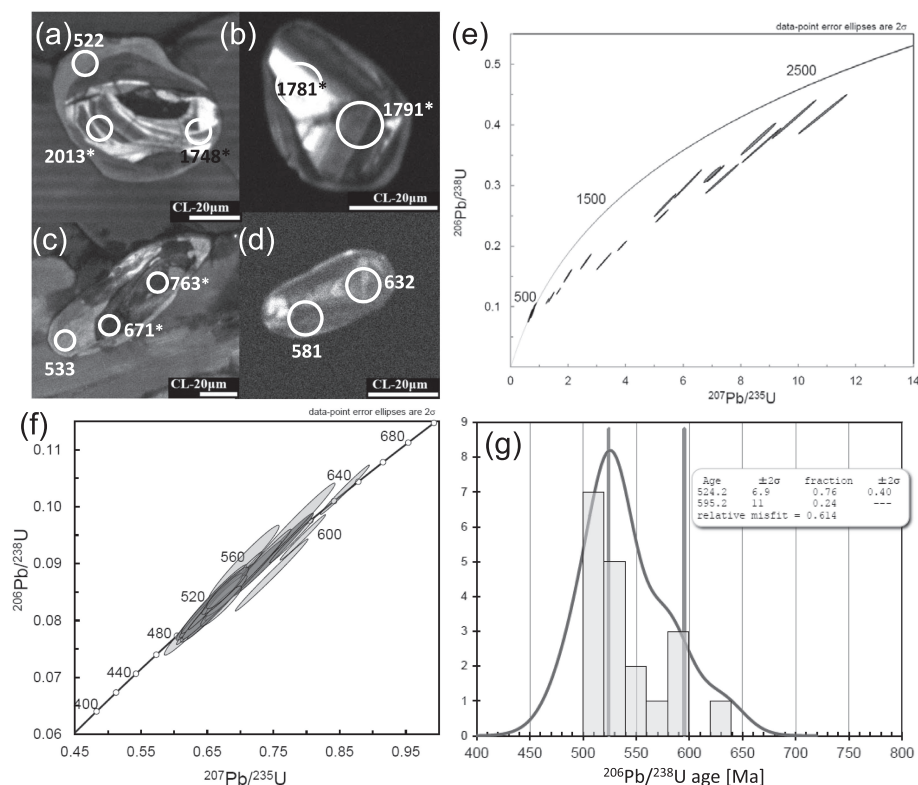
Figure 10. (a)-(d) CL images of zircon dated by the LA-ICPMS. Circles represent the analysis points. Numbers represent the $^{206}Pb/^{238}U$ age of concordant points, and numbers with '*' represents discordant data. (a) Zircon Z-18 in the matrix. (b) Zircon Z-4 included in the garnet A. (c) Zircon Z-9 in the matrix. (d) Zircon Z-7 included in the garnet C. (e) Concordia diagram for the LA-ICPMS U-Pb zircon dating. (f) Enlargement of ~ 500 Ma part in (e). (g) A probability density plot of the concordant data in (f). (e)-(g) Calculated and plotted by Isoplot 4.15 (Ludwig, 2012). Color version of Figure 10 is available online from http://doi.org/10.2465/jmps.150812.

affected by the diffusion of Pb and partial resetting of the U-Th-Pb system under high-temperature conditions (e.g., Suzuki et al., 1994; Kawakami and Suzuki, 2011).

Possible polymetamorphism in the Skallen and Skallevikshalsen areas of the LHC

The P-rich patch in the garnet core of the garnet-sillimanite gneiss from Skallevikshalsen was previously interpreted as three-dimensionally continuous to the P-rich rim, and appears in the core because of the cutting effect (Kawakami and Hokada, 2010). The present study revealed that one of the P-rich patches shows high Cr and HREE concentrations than the P-rich garnet rim. Because the trace element concentrations of the P-rich patch are, for most elements, between that of surrounding P-poor garnet core and that of the P-rich rim (Fig. 7), it is possible to interpret that the P-rich patch is continuous to the rim as previously considered, and that the diffuse nature of the patch observed for some trivalent elements (Figs. 2d-2f) is a result of diffusion after the patch and the garnet rim growths.

However, an isotope map by ^{51}V (Fig. 2d) conflicts with this interpretation, because the garnet rim and the patch has distinctly different ^{51}V concentration. Absence of diffusive zoning in ^{51}V at the core/rim boundary of garnet also suggests that the core and rim did not have significant difference in ^{51}V concentration as observed

between the ^{51}V-poor patch and the garnet core. Therefore, there is a chance to consider that the P-rich (^{51}V-poor) patch is not continuous with the garnet rim, and is originally different in composition. That is, another probable interpretation is that this part represents a relic of the preexisted garnet. Since the P-rich patch includes kyanite, the precursor rock can be a medium- to high-pressure type metamorphic rock. Presence of the older age population monazites in Skallevikshalsen and Skallen (Hokada and Motoyoshi, 2006), in addition to the possible relic garnet in Skallevikshalsen, suggest that rocks in these areas experienced polymetamorphism, and resetting by the ~ 560-500 Ma metamorphic event was incomplete.

Taking into account the presence of Cl-rich biotite inclusions in garnet, infiltration of brine that triggered partial melting is one probable event that took place during ~ 560-500 Ma metamorphism in the Skallevikshalsen area. It is known from experimental study that $CaCl_2$-bearing fluid can recrystallize monazite through dissolution-precipitation mechanism and make newly grown monazite Th-richer (Seydoux-Guillaume et al., 2002). Although the effect of the partial melting to the fluid-monazite reaction is unclear in the present case, Th-richer composition of the younger age population monazite may be explained if the infiltration of brine is considered. Therefore, possibility of polymetamorphism and role of fluids including brines should be carefully considered in the future study of the LHC.

Recognizing the timing of fluid release/infiltration during metamorphism and crystallization of plutonic bodies, and understanding the composition of fluids is of great importance especially because brines are able to recrystallize datable minerals such as monazite and rarely zircon (e.g., Seydoux-Guillaume et al., 2002; Kawakami and Suzuki, 2011; Higashino et al., 2013), which makes the interpretation of geochronological data more complex (e.g., Kawakami et al., 2014). More reliable interpretation of zircon and monazite dating in high-grade metamorphic rocks is required to understand the rate and duration of crustal processes. As presented in this study, detailed microstructural observation using trace element mapping combined with detailed petrography especially focusing on the Cl-bearing minerals as a tracer of Cl-rich fluids would become a powerful tool in the future studies.

ACKNOWLEDGMENTS

SUPPLEMENTARY MATERIALS

Tables 2 and 3, Supplementary Tables S1-S3, and color version of Figures 6, 7, 9, and 10 are available online from http://doi.org/10.2465/jmps.150812.

REFERENCES

Aranovich, L.Y., Newton, R.C. and Manning, C.E. (2013) Brine-assisted anatexis: Experimental melting in the system haplogranite-H_2O-NaCl-KCl at deep-crustal conditions. Earth and Planetary Science Letters, 374, 111-120.

Cesare, B., Ferrero, S., Salvioli-Mariani, E., Pedron, D. and Cavallo, A. (2009) 'Nanogranite' and glassy inclusions: The anatectic melt in migmatites and granulites. Geology, 37, 627-630.

Chevychelov, V.Y., Botcharnikov, R.E. and Holtz, F. (2008) Partitioning of Cl and F between fluid and hydrous phonolitic melt of Mt. Vesuvius at ~ 850-1000 °C and 200 MPa. Chemical

Geology, 256, 172-184.

Dunkley, D.J. (2007) Isotopic zonation in zircon as a recorder of progressive metamorphism. Goldschmidt Conference Abstracts 2007, A244.

Ferry, J.M. and Watson, E.B. (2007) New thermodynamic models and revised calibrations for the Ti-in-zircon and Zr-in-rutile thermometers. Contributions to Mineralogy and Petrology, 154, 429-437.

Filiberto, J., Treiman, A.H., Giesting, P.A., Goodrich, C.A. and Gross, J. (2014) High-temperature chlorine-rich fluid in the Martian crust: A precursor to habitability. Earth and Planetary Science Letters, 401, 110-115.

Harley, S.L. and Kelly, N.M. (2007) The impact of zircon-garnet REE distribution data on the interpretation of zircon U-Pb ages in complex high-grade terrains: An example from the Rauer Islands, East Antarctica. Chemical Geology, 241, 62-87.

Harley, S.L. and Nandakumar, V. (2014) Accessory mineral behaviour in granulite migmatites: a case study from the Kerala Khondalite Belt, India. Journal of Petrology, 55, 1965-2002.

Harlov, D.E. and Forster, H.-J. (2002) High-grade fluid metasomatism on both a local and regional scale: the Seward Penninsula, Alaska and the Ivrea-Verbano Zone, Northern Italy. Part I: Petrography and silicate mineral chemistry. Journal of Petrology, 45, 769-799.

Heinrich, W. (2007) Fluid immiscibility in metamorphic rocks. In Fluid-Fluid Interactions (Liebscher, A. and Heinrich, A.C. Eds.). Reviews in Mineralogy and Geochemistry, 65, 389-430.

Higashino, F., Kawakami, T., Satish-Kumar, M., Ishikawa, M., Maki, K., Tsuchiya, N., Grantham, G.H. and Hirata, T. (2013) Chlorine-rich fluid or melt activity during granulite facies metamorphism in the Late Proterozoic to Cambrian continental collision zone - an example from the Sør Rondane Mountains, East Antarctica. Precambrian Research, 234, 229-246.

Higashino, F., Kawakami, T., Tsuchiya, N., Satish-Kumar, M., Ishikawa, M., Grantham, G.H., Sakata, S., Hattori, K. and Hirata, T. (2015) Geochemical behavior of zirconium during Cl-rich fluid or melt infiltration under upper amphibolite facies metamorphism — A case study from Brattnipene, Sør Rondane Mountains, East Antarctica. Journal of Mineralogical and Petrological Sciences, 110, 166-178.

Hiroi, Y., Shiraishi, K., Nakai, Y., Kano, T. and Yoshikura, S. (1983a) Geology and petrology of Prince Olav Coast, East Antarctica. In Antarctic Earth Science Fourth International Symposium (Oliver, R.L. Jsgo, J.B. Eds.). Australian Academy of Science, Canberra, 32-35.

Hiroi, Y., Shiraishi, K., Yanai, K. and Kizaki, K. (1983b) Aluminum silicates in the Prince Olav and Soya Coasts, East Antarctica. Memoirs of National Institute for Polar Research, Special Issue, 28, 115-131.

Hiroi, Y., Shiraishi, K., Motoyoshi, Y., Kanisawa, S., Yanai, K. and Kizaki, K. (1986) Mode of occurrence, bulk chemical compositions, and mineral textures of ultramafic rocks in the Lützow-Holm Complex, East Antarctica. Memoirs of National Institute for Polar Research, Special Issue, 43, 62-84.

Hiroi, Y., Shiraishi, K. and Motoyoshi, Y. (1991) Late Proterozoic paired metamorphic complexes in East Antarctica, with special reference to the tectonic significance of ultramafic rocks. In Geological Evolution of Antarctica (Thomson, M.R.A., Crane, J.A. and Thomson, J.W. Eds.). Cambridge University Press, Cambridge, 83-87.

Hiroi, Y., Yanagi, A., Kato, M., Kobayashi, T., Prame, B., Hokada, T., Satish-Kumar, M., Ishikawa, M., Adachi, T., Osanai, Y., Motoyoshi, Y. and Shiraishi, K. (2014) Supercooled melt inclusions in lower-crustal granulites as a consequence of rapid exhumation by channel flow. Gondwana Research, 25, 226-234.

Hokada, T. and Motoyoshi, Y. (2006) Electron microprobe technique for U-Th-Pb and REE chemistry of monazite, and its implications for pre-, peak- and post-metamorphic events of the Lützow-Holm Complex and the Napier Complex, East Antarctica. Polar Geoscience, 19, 118-151.

Icenhower, J. and London, D. (1997) Partitioning of fluorine and chlorine between biotite and granitic melt: experimental calibration at 200 MPa H_2O. Contributions to Mineralogy and Petrology, 127, 17-29.

Ishikawa, M., Motoyoshi, Y., Fraser, G.L. and Kawasaki, T. (1994) Structural evolution of Rundvågshetta region, Lützow-Holm Bay, East Antarctica. Proceedings of the NIPR Symposium on Antarctic Geosciences, 7, 69-89.

Johnson, M.R.W. and Harley, S.L. (2012) Orogenesis: The making of the mountains. pp. 388, Cambridge, Cambridge University Press.

Kato, M. (2013) Partial melting of alternation of pelitic silicate rocks and carbonate rocks: interaction between different rock types in the deep crust. Doctoral thesis, Chiba University, Japan.

Kawakami, T. and Ikeda, T. (2004) Timing of ductile deformation and peak metamorphism in Skallevikshalsen, Lützow-Holm Complex, East Antarctica. Polar Geoscience, 17, 1-11.

Kawakami, T. and Motoyoshi, Y. (2004) Timing of attainment of the spinel + quartz coexistence in garnet-sillimanite leucogneiss from Skallevikshalsen, Lützow-Holm Complex, East Antarctica. Journal of Mineralogical and Petrological Sciences, 99, 311-319.

Kawakami, T., Ellis, D.J. and Christy, A.G. (2006) Sulfide evolution in high-temperature to ultrahigh temperature metamorphic rocks from Lützow-Holm Complex, East Antarctica. Lithos, 92, 431-446.

Kawakami, T., Grew, E.S., Motoyoshi, Y., Shearer, C.K., Ikeda, T., Burger, P.V. and Kusachi, I. (2008) Kornerupine *sensu stricto* associated with mafic and ultramafic rocks in the Lützow-Holm Complex at Akarui Point, East Antarctica: What is the source of boron? In Geodynamic Evolution of East Antarctica: A Key to the East-West Gondwana Connection (Satish-Kumar, M. et al. Eds.). Geological Society, London, Special Publications, 308, 351-375.

Kawakami, T. and Hokada, T. (2010) Linking *P-T* path with development of discontinuous phosphorus zoning in garnet during high-temperature metamorphism — an example from Lützow-Holm Complex, East Antarctica. Journal of Mineralogical and Petrological Sciences 105, 175-186.

Kawakami, T. and Suzuki, K. (2011) CHIME monazite dating as a tool to detect polymetamorphism in high temperature metamorphic terrane: Example from the Aoyama area, Ryoke metamorphic belt, Southwest Japan. Island Arc, 20, 439-453.

Kawakami, T., Yamaguchi, I., Miyake, A., Shibata, T., Maki, K., Yokoyama, D.T. and Hirata, T. (2013) Behavior of zircon in the upper-amphibolite to granulite facies schist/migmatite transition, Ryoke metamorphic belt, SW Japan: constraints from the melt inclusions in zircon. Contributions to Mineralogy and Petrology, 165, 575-591.

Kawakami, T., Nakano, N., Higashino, F., Hokada, T., Osanai, Y.,

Yuhara, M., Charusiri, P., Yonemura, K., Kamikubo, H. and Hirata, T. (2014) U-Pb zircon and CHIME monazite dating of granitoids and high-grade metamorphic rocks from the Eastern and Peninsular Thailand — A new report of Early Paleozoic granite. Lithos, 200-201, 64-79.

Kawasaki, T., Ishikawa, M. and Motoyoshi, Y. (1993) A preliminary report on cordierite-bearing assemblages from Rundvågshetta region, Lützow-Holm Bay, East Antarctica. Proceedings of the NIPR Symposium on Antarctic Geosciences, 6, 47-56.

Kawasaki, T., Adachi, T., Nakano, N. and Osanai, Y. (2013) Possible armalcolite pseudomorph-bearing garnet-sillimanite gneiss from Skallevikshalsen, Lützow-Holm Complex, East Antarctica: Implications for ultrahigh-temperature metamorphism. In Antarctica and Supercontinent Evolution (Harley, S.L., Fitzsimons, I.C.W. and Zhao, Y. Eds.). Geological Society, London, Special Publications, 383, 135-167.

Korhonen, F.J., Clark, C., Brown, M., Bhattacharya, S. and Taylor, R. (2013) How long-lived is ultrahigh temperature (UHT) metamorphism? Constraints from zircon and monazite geochronology in the Eastern Ghats orogenic belt, India. Precambrian Research, 234, 322-350.

Kretz, R. (1983) Symbols for rock-forming minerals. American Mineralogist 68, 277-279.

Kullerud, K. (1995) Chlorine, titanium and Barium-rich biotites: factors controlling biotite composition and the implications for garnet-biotite geothermometry. Contributions to Mineralogy and Petrology 120, 42-59.

Ludwig, K.R. (2012) User's manual for *Isoplot 3.75*. A geological toolkit for Microsoft Excel. pp. 75, Berkeley Geochronology Center Special Publication No.5 (revision of January 30, 2012).

Markl, G. and Bucher, K. (1998) Composition of fluids in the lower crust inferred from metamorphic salt in lower crustal rocks. Nature, 391, 781-783.

Motoyoshi, Y. and Ishikawa, M. (1997) Metamorphic and structural evolution of granulites from Rundvågshetta, Lützow-Holm Bay, East Antarctica. In The Antarctic Region: Geological Evolution and Processes (Ricci, C.A. Ed.). Terra Antarctica Publication, Siena, 65-72.

Munoz, J.L. (1992) Calculation of HF and HCl fugacities from biotite compositions: revised equations. Geological Society of America, Abstract with Programs, 24, A221.

Munoz, J.L. and Swenson, A. (1981) Chloride-hydroxyl exchange in biotite and estimation of relative HCl/HF activities in hydrothermal fluids. Economic Geology, 76, 2212-2221.

Newton, R.C., Aranovich, L. Ya., Hansen, E.C. and Vandenheuvel, B.A. (1998) Hypersaline fluids in Precambrian deep-crustal metamorphism. Precambrian Research, 91, 41-63.

Newton, R.C. and Manning, C.E. (2010) Role of saline fluids in deep-crustal and upper-mantle metasomatism: insights from experimental studies. Geofluids, 10, 58-72.

Pattison, D.R.M. (1992) Stability of andalusite and sillimanite and the Al_2SiO_5 triple point: constraints from the Ballachulish aureole, Scotland. Journal of Geology, 100, 423-446.

Piccoli, P.M. and Candela, P.A. (1994) Apatite in felsic rocks, a model for the estimation of initial halogen concentrations in the Bishop Tuff (Long Valley) and Tuolumne Intrusive Suite (Sierra Nevada Batholith) magmas. American Journal of Science 294, 92-135.

Rubatto, D. (2002) Zircon trace element geochemistry: partitioning with garnet and the link between U-Pb ages and metamor-

phism. Chemical Geology, 184, 123-138.

Rubatto, D., Williams, I.S. and Buick, I.S. (2001) Zircon and monazite response to prograde metamorphism in the Reynolds Range, central Australia. Contributions to Mineralogy and Petrology, 140, 458-468.

Rubatto, D., Chakraborty, S. and Dasgupta, S. (2013) Timescales of crustal melting in the Higher Himalayan Crystallines (Sikkim, Eastern Himalaya) inferred from trace element-constrained monazite and zircon chronology. Contributions to Mineralogy and Petrology, 165, 349-372.

Rubenach, M.J. (2005) Relative timing of albitization and chlorine enrichment in biotite in Proterozoic schists, Snake Creek anticline, Mount Isa inlier, Northeastern Australia. The Canadian Mineralogist, 43, 349-366.

Sambridge, M.S. and Compston, W. (1994) Mixture modeling of multi-component data sets with application to ion-probe zircon ages. Earth and Planetary Science Letters, 128, 373-90.

Satish-Kumar, M. and Wada, H. (2000) Carbon isotopic equilibrium between calcite and graphite in Skallen Marbles, East Antarctica: Evidence for preservation of peak metamorphic temperatures. Chemical Geology, 166, 173-182.

Satish-Kumar, M., Hermann, J., Tsunogae, T. and Osanai, Y. (2006) Carbonation of Cl-rich scapolite boudins in Skallen, East Antarctica: evidence for changing fluid condition in the continental crust. Journal of Metamorphic Geology, 24, 241-261.

Satish-Kumar, M., Hokada, T., Kawakami, T. and Dunkley, D.J. (2008a) Geosciences research in East Antarctica (0°E-60°E): present status and future perspectives. Geological Society, London, Special Publications, 308, 1-20.

Satish-Kumar, M., Miyamoto, T., Hermann, J., Kagami, H., Osanai, Y. and Motoyoshi, Y. (2008b) Pre-metamorphic carbon, oxygen and strontium isotope signature of high-grade marbles from the Lützow-Holm Complex, East Antarctica: apparent age constraints of carbonate deposition. In Geodynamic Evolution of East Antarctica: A Key to the East-West Gondwana Connection (Satish-Kumar, M. et al. Eds.). Geological Society, London, Special Publications, 308, 147-164.

Selby, D. and Nesbitt, B.E. (2000) Chemical composition of biotite from the Casino porphyry Cu-Au-Mo mineralization, Yukon, Canada: evaluation of magmatic and hydrothermal fluid chemistry. Chemical Geology 171, 77-93.

Shinohara, H., Iiyama, J.T. and Matsuo, S. (1989) Partition of chlorine compounds between silicate melt and hydrothermal solutions: I. Partition of NaCl-KCl. Geochimica et Cosmochimica Acta, 53, 2617-2630.

Shiraishi, K., Ellis, D.J., Hiroi, Y., Fanning, C.M., Motoyoshi, Y. and Nakai, Y. (1994) Cambrian orogenic belt in East Antarctica and Sri Lanka: Implications for Gondwana Assembly. Journal of Geology, 102, 47-65.

Shiraishi, K., Dunkley, D.J., Hokada, T., Fanning, C.M., Kagami, H. and Hamamoto, T. (2008) Geochronological constraints on the Late Proterozoic to Cambrian crustal evolution of eastern Dronning Maud Land, East Antarctica: a synthesis of SHRIMP U-Pb age and Nd model age data. In Geodynamic Evolution of East Antarctica: A Key to the East-West Gondwana Connection (Satish-Kumar, M. et al. Eds.). Geological Society of London Special Publications, 308, 21-67.

Shmulovich, K.I. and Graham, C.M. (1999) An experimental study of phase equilibria in the system H_2O-CO_2-NaCl at 800 °C and 9 kbar. Contributions to Mineralogy and Petrology, 136, 247-257.

Shmulovich, K.I. and Graham, C.M. (2004) An experimental study of phase equilibria in the systems H_2O-CO_2-$CaCl_2$ and H_2O-CO_2-NaCl at high pressures and temperatures (500-800 °C, 0.5-0.9 GPa): geological and geophysical applications. Contributions to Mineralogy and Petrology, 146, 450-462.

Smit, C.A. and Van Reenen, D.D. (1997) Deep crustal shear zones, high-grade tectonites, and associated metasomatic alteration in the Limpopo belt, South Africa: implications for deep crustal processes. Journal of Geology, 105, 37-57.

Seydoux-Guillaume, A.M., Paquette, J.L., Wiedenbeck, M., Montel, J.M. and Heinrich, W. (2002) Experimental resetting of the U-Th-Pb system in monazite. Chemical Geology, 191, 165-181.

Suzuki, K., Adachi, M. and Kajizuka, I. (1994) Electron microprobe observations of Pb diffusion in metamorphosed detrital monazites. Earth and Planetary Science Letters, 128, 391-405.

Tomkins, H.S., Powell, R. and Ellis, D.J. (2007) The pressure dependence of the zirconium-in-rutile thermometer. Journal of Metamorphic Geology, 25, 703-713.

Touret, J.L.R. and Huizenga, J.-M. (2011) Fluids in granulites. In Origin and Evolution of Precambrian High-Grade Gneiss Terranes, with Special Emphasis on the Limpopo Complex of Southern Africa (Van Reenen, D.D. et al. Eds.). The Geological Society of America Memoir, 207, 25-37.

Trommsdorff, V., Skippen, G. and Ulmer, P. (1985) Halite and sylvite as solid inclusions in high-grade metamorphic rocks. Contributions to Mineralogy and Petrology, 89, 24-29.

Van den Berg, R. and Huizenga, J.M. (2001) Fluids in granulites of the Southern Marginal Zone of the Limpopo Belt, South Africa. Contributions to Mineralogy and Petrology 141, 529-545.

Webster, J.D., Tappen, C.M. and Mandeville, C.W. (2009) Partitioning behavior of chlorine and fluorine in the system apatite-melt-fluid. II: Felsic silicate systems at 200 MPa. Geochimica et Cosmochimica Acta, 73, 559-581.

Weinberg, R.F. and Hasalová, P. (2015) Water-fluxed melting of the continental crust: A review. Lithos, 212-215, 158-188.

Yoshida, M., Yoshida, Y., Ando, H., Ishikawa, T. and Tatsumi, T. (1976) Explanatory text of geological map of Skallen, Antarctica. Antarctic geological map series, Sheet 9, Skallen. National Institute of Polar Research, pp. 16.

Yoshimura, Y., Motoyoshi, Y., Miyamoto, T., Grew, E.S., Carson, C.J. and Dunkley, D.J. (2004) High-grade metamorphic rocks from Skallevikshalsen in the Lützow-Holm Complex, East Antarctica: metamorphic conditions and possibility of partial melting. Polar Geoscience, 17, 57-87.

Yoshimura, Y., Motoyoshi, Y. and Miyamoto, T. (2008) Sapphirine + quartz association in garnet: Implication for ultrahigh-temperature metamorphism in Rundvågshetta, Lützow-Holm Complex, East Antarctica. In Geodynamic Evolution of East Antarctica: A Key to the East-West Gondwana Connection (Satish-Kumar, M. et al. Eds.). Geological Society, London, Special Publications, 308, 377-390.

Zack, T., Moraes, A.R. and Kronz, A.A. (2004) Temperature dependence of Zr in rutile: empirical calibration of a rutile thermometer. Contributions to Mineralogy and Petrology, 148, 471-488.